Characterizing Surface Wetting and Interfacial Properties using Enhanced Sampling (SWIPES)[†]

Hao Jiang, [a] Suruchi Fialoke, [a] Zachariah Vicars, [a] and Amish J. Patel [a]

Abstract

We introduce an accurate and efficient method for characterizing surface wetting and interfacial properties, such as the contact angle made by a liquid droplet on a solid surface, and the vapor-liquid surface tension of a fluid. The method makes use of molecular simulations in conjunction with the indirect umbrella sampling technique to systematically wet the surface and estimate the corresponding free energy. To illustrate the method, we study the wetting of a family of Lennard-Jones surfaces by water. For surfaces with a wide range of attractions for water, we estimate contact angles using our method, and compare them with contact angles obtained using droplet shapes. Notably, our method is able to capture the transition from partial to complete wetting as surface – water attractions are increased. Moreover, the method is straightforward to implement and is computationally efficient, providing accurate contact angle estimates in roughly 5 nanoseconds of simulation time.

A. Introduction

Wetting of solid surfaces by fluids is important in diverse disciplines, including but not limited to surface chemistry, materials characterization, oil and gas recovery[1–5]. In general, the wettability of a solid by a fluid is characterized by a wetting coefficient, $k \equiv (\gamma_{SV} - \gamma_{SL})/\gamma_{VL}$, where γ represents surface tension, and the subscripts correspond to the coexisting vapor (V), liquid (L) and solid (S) phases. The wetting coefficient is also related to the contact angle (θ) that a liquid droplet (surrounded by its vapor) makes with a solid surface; according to Young's equation, $\cos\theta = (\gamma_{SV} - \gamma_{SL})/\gamma_{VL} = k$. Thus, the extent to which a fluid prefers to wet a solid, or the preference of the solid for the liquid over its vapor, can be characterized by estimating either k or θ.

The most common approach for characterizing wettability is the direct measurement of contact angle using the so-called sessile droplet method, wherein θ is determined from the geometry of a liquid droplet supported by a solid surface. Although the sessile droplet method is usually associated with the experimental determination of θ, molecular simulations have also made extensive use of this method. Indeed, both molecular dynamics (MD) and Monte Carlo (MC) simulations have been used to estimate contact angles for diverse interfacial systems, ranging from toy models[6–10] to realistic molecular models such as water/minerals[11–17] and textured surfaces[18–20]. However, in contrast with the millimeter-sized sessile droplets used in experiments, the droplets used in molecular simulations are nanoscopic. At the nanoscale, the geometry of spherical droplets can be influenced by the tension associated with the three-phase contact line, which causes the estimated θ to depend on droplet size[21,22]. Although estimates of θ have been shown to depend strongly on droplet size in some instances[23,24], they have been found to be remarkably unaffected by droplet size in other instances[25,26]. Line tension effects can also be mitigated by using a cylindrical droplet that is infinitely long (due to periodic boundaries), because the three-phase contact line then has a fixed length and is independent of droplet size[27]. However, a number of studies have recently shown that θ extracted from the geometry of such cylindrical droplets can nevertheless depend on the curvature of the droplet[28–30]. In addition to the challenges posed by line tension and finite size effects, the determination of θ from droplet geometry is also plagued by a certain degree of ambiguity regarding the exact location of the solid-fluid interface[31–33]. Each of these effects can be mitigated by increasing droplet size; however, given that neither the magnitude of these effects, nor their dependence on surface characteristics is well understood, it can be challenging to determine the size of the droplet that must be simulated to estimate θ with a certain accuracy.

To address these challenges, a number of free energy methods have been proposed for estimating k[34–38]. The interface potential approach involves estimating the free energy per unit area needed: (i) to wet a surface in contact with vapor, $\gamma_{VL} + \gamma_{SL} - \gamma_{SV} = \gamma_{VL}(1 - k)$ (spreading potential), and (ii) to dewet a surface in contact with liquid, $\gamma_{VL} + \gamma_{SV} - \gamma_{SL} = \gamma_{VL}(1 + k)$ (drying potential), thereby providing estimates of both γ_{VL} and k[34]. Errington and co-workers have illustrated the utility of this approach, and have employed it extensively in conjunction with grand canonical Monte Carlo simulations to study the wetting properties of

diverse surfaces by a number of fluids[34,39,40]. However, because using grand canonical Monte Carlo to simulate large or complex fluid molecules can be inefficient, and performing molecular dynamics simulations in the grand canonical ensemble is cumbersome, the interface potential method has not been applied to the study of such complex fluids. To this end, approaches that employ molecular dynamics simulations have been developed, e.g., the phantom-wall and dry-surface methods by Leroy and Muller-Plathe[35-37]. These approaches are similar in spirit to the drying potential described above, i.e., they employ processes for estimating the work of adhesion. In the phantom-wall method, a structureless repulsive wall is employed to push the liquid away from the surface of interest[35,36], whereas in the dry-surface method, surface-water attractions are turned off reversibly[37]. These methods have been widely applied to calculate wetting properties[35,41-43]. However, in each of the above free energy methods, the solid-liquid interface is replaced by both a solid-vapor and a vapor-liquid interface[34-36,44]. Such formation of vapor-liquid interfaces in the presence of periodic boundary conditions involves transitions between dewetted morphologies[45-47], which can give rise to hysteresis and complicate estimation of the associated free energies[48-50].

Moreover, in the phantom-wall method, a solid-liquid interface is replaced not by a solid-vapor interface, but by a solid-vacuum interface. The corresponding free energy per unit area, $\gamma_{VL} + \gamma_{S,Vac} - \gamma_{SL}$ approximates $\gamma_{VL} + \gamma_{SV} - \gamma_{SL} = \gamma_{VL}(1 + k)$ if the solid-vacuum surface tension, $\gamma_{S,Vac} \approx \gamma_{SV}$. Such an assumption is reasonable when solid-fluid attractions are relatively weak, and there little to no adsorption from the vapor phase onto the solid surface. However, $\gamma_{S,Vac}$ is expected to differ substantially from γ_{SV} when the solid-fluid attractions are significant. Indeed, Kanduč and Netz[51,52] have recently shown that for a sufficiently solvophilic surface, there is substantial adsorption from the vapor phase onto the solid surface, which lowers γ_{SV} (relative to $\gamma_{S,Vac}$). To do so, the authors introduced a free energy method that enables estimation of the spreading potential, and is able to capture the transition from partial to complete wetting as solid-fluid attractions are increased. However, the method is computationally demanding and requires roughly 50 simulations for each estimate of k.

Here, we introduce a versatile and computationally efficient method, which we call "Surface Wetting and Interfacial Properties using Enhanced Sampling" or SWIPES. SWIPES makes use of the indirect umbrella sampling (INDUS) technique[53,54] to systematically wet the surface of interest, and estimate the free energy change associated with the process. It can be used in conjunction with molecular dynamics simulations to obtain estimates of not just wet-

ting coefficients k, but also of vapor-liquid surface tensions, γ_{VL}. We illustrate SWIPES by using it to study the wetting of Lennard-Jones (LJ) surfaces by SPC/E water[55]. We estimate wetting coefficients for surfaces with a wide range of solid-water attractions, and compare our results with those obtained from droplet geometries. We also show that our method is capable of capturing the transition from partial to complete wetting as the solid-water affinity is increased. The rest of the paper is organized as follows: In section B, our approach for estimating wetting coefficients is described. Details pertaining to the molecular models used and the simulation methods employed are given in section C. In section D, contact angles calculated from free energies and from droplet geometries are compared, and the transition from partial to complete wetting as well as the computational efficiency of the method are discussed. Finally, we summarize our findings in the conclusions section.
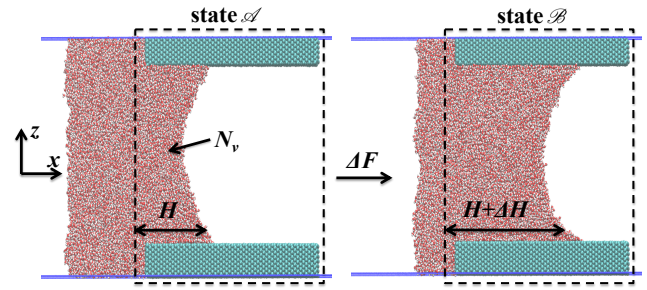

Fig. 1 Schematic illustrating our approach. The solid surface of interest is represented using cyan spheres. The dashed line marks the observation volume, v. The number of fluid molecules (in this case water, shown in red and white) inside the observation volume is denoted by N_v. A biasing potential is used to modulate N_v, which results in the vapor-liquid interface moving along the solid surface by a distance ΔH. The wetting coefficient (k) and the contact angle (θ) can be obtained from estimates of ΔH, and the free energy change associated with this process, ΔF; see Equation 3.

B. Estimating Wetting Coefficients

In this section, we describe our approach for calculating the wetting coefficient, k, defined as:

$$k \equiv \frac{\gamma_{SV} - \gamma_{SL}}{\gamma_{VL}} \qquad (1)$$

The wetting coefficient is related to the contact angle (θ) through $k = \cos\theta$.

1. Outline of Our Approach

To estimate k for the wetting of a flat solid surface by a liquid in equilibrium with its vapor, we employ the schematic shown in Figure 1. As the number of waters, N_v, in the observation volume, v, increases, and the system moves from state $\mathscr{A}$ to state $\mathscr{B}$, the area of the solid wetted by the liquid increases by $\Delta A = 2L\Delta H$, where L is the length of the simulation box in the direction perpendicular to the page, and

ΔH is the distance that the vapor-liquid interface advances along the solid. The reversible work that must be done to wet the solid as the system moves from state $\mathscr{A}$ to state $\mathscr{B}$, and the corresponding change in system free energy, ΔF, is given by

$$\Delta F = (\gamma_{\text{SL}} - \gamma_{\text{SV}})\Delta A = -k\gamma_{\text{VL}}\Delta A = -k\gamma_{\text{VL}} \cdot 2L\Delta H. \quad (2)$$

Although a (curved) vapor-liquid interface and three-phase contact lines are present in our setup, the corresponding interfacial area, its curvature, and the contact line length are all unaffected by the advance of the liquid slab along the solid surface, and thereby do not influence ΔF. The wetting coefficient (k) or the contact angle (θ) can thus be estimated from the ratio of ΔF and ΔH as

$$k = \cos\theta = -\frac{1}{2\gamma_{\text{VL}}L} \cdot \frac{\Delta F}{\Delta H}. \quad (3)$$

We note that the ratio $\Delta F/\Delta H$ ought to be the same ($-2\gamma_{\text{VL}}Lk$), regardless the positions of vapor-liquid interface in state $\mathscr{A}$ and state $\mathscr{B}$, as long as the solid surface under consideration is homogeneous, and k is a well-defined constant.

2. Indirectly Sampling $\tilde{N}_v$

To efficiently estimate $\Delta F/\Delta H$, we employ enhanced sampling simulations that pull waters into v and wet the surface. In principle, this can be accomplished by biasing the number of waters, N_v, in the rectangular observation volume, v, shown by the dashed lines in Figure 1. In practice, because N_v is a discrete function of particle positions, $\overline{\mathbf{R}}$, biasing it using molecular dynamics simulations would result in impulsive forces. We therefore bias N_v indirectly by instead biasing a coarse-grained number of fluid molecules, $\tilde{N}_v$, following the indirect umbrella sampling (INDUS) prescription[53,54]; $\tilde{N}_v$ is closely related to N_v, but is a continuous function of $\overline{\mathbf{R}}$. The precise definition of $\tilde{N}_v$ and its dependence on $\overline{\mathbf{R}}$ can be found in the ref. 54. Our choice of the location of v is discussed in further detail in the Supplementary Information.

3. Biased Simulations to Wet the Surface

We choose a biasing potential that is parabolic in $\tilde{N}_v(\overline{\mathbf{R}})$,

$$U_{\kappa,N^*}(\tilde{N}_v) = \frac{\kappa}{2}(\tilde{N}_v - N^*)^2, \quad (4)$$

with κ and N^* parametrizing the potential. We further choose state $\mathscr{A}$ and state $\mathscr{B}$ to correspond to biased ensembles with different values of N^*, say N_A^* and N_B^*. Although this choice is convenient, it is certainly not unique; alternative definitions can be chosen for the two states, e.g., constant-$\tilde{N}_v$ ensembles with different $\tilde{N}_v$-values. Nevertheless, this choice enables us to reversibly wet the surface,

and to estimate the corresponding free energetics, which we characterize using the free energy difference between the biased and unbiased ensembles, F_{κ,N^*}. Similarly, to characterize the position of the vapor-liquid interface, H, we employ the biased ensemble average of the center of mass of water in the simulation box in the direction (x) perpendicular to the vapor-liquid interface, i.e., $H \equiv \langle x_{\text{COM}} \rangle_{\kappa,N^*}$, where $\langle \mathscr{O}(\overline{\mathbf{R}}) \rangle_{\kappa,N^*}$ represents the average of $\mathscr{O}(\overline{\mathbf{R}})$ in the biased ensemble. As shown in the Supplementary Information, both the position of the vapor-liquid interface, H, and the corresponding free energy, F_{κ,N^*}, vary linearly with N^*; i.e., both $f \equiv dF_{\kappa,N^*}/dN^*$ and $h \equiv dH/dN^*$ are independent of N^*. Briefly, this stems from the fact that the balance of forces at the 3-phase contact line is governed entirely by the corresponding interfacial tensions, and the shape of the vapor-liquid interface is independent of the biasing potential. Thus, the ratio $\Delta F/\Delta H$ needed to obtain k (using Equation 3) can be estimated as a ratio of the corresponding slopes, i.e.,

$$\frac{\Delta F}{\Delta H} = \frac{dF_{\kappa,N^*}/dN^*}{dH/dN^*} = \frac{f}{h} \quad (5)$$

4. Estimating f and h

To estimate f, we use the thermodynamic integration formula,

$$f \equiv \frac{dF_{\kappa,N^*}}{dN^*} = \left\langle \frac{dU_{\kappa,N^*}}{dN^*} \right\rangle_{\kappa,N^*} = \kappa[N^* - \langle \tilde{N}_v \rangle_{\kappa,N^*}]. \quad (6)$$

Thus, f can be obtained using a single simulation through

$$f = -\kappa[\langle \tilde{N}_v \rangle_{\kappa,N^*} - N^*]. \quad (7)$$

Alternatively, by rearranging Equation 7, we get

$$\langle \tilde{N}_v \rangle_{\kappa,N^*} = N^* - f/\kappa, \quad (8)$$

suggesting that $\langle \tilde{N}_v \rangle_{\kappa,N^*}$ ought to differ from N^* by a constant offset, $-f/\kappa$. Thus, an alternate way to estimate f from multiple simulations (with the same κ but different N^*-values) would be to plot $\langle \tilde{N}_v \rangle_{\kappa,N^*}$ versus N^*; the data can then be fitted to a straight line with a unit slope, and the y-intercept used to estimate $-f/\kappa$. This procedure is functionally equivalent to averaging estimates of f obtained from different biased simulations using Equation 7.

Similarly, h can be obtained from multiple biased simulations (with the same κ) by fitting $H \equiv \langle x_{\text{COM}} \rangle_{\kappa,N^*}$ versus N^* to a straight line, and obtaining the slope. Alternatively, h can also be obtained from a single simulation using the co-variance relation

$$h \equiv \frac{dH}{dN^*} = \frac{d\langle x_{\text{COM}} \rangle_{\kappa,N^*}}{dN^*} = \beta\kappa\langle \delta x_{\text{COM}} \delta N_v \rangle_{\kappa,N^*}, \quad (9)$$

where $\beta^{-1} \equiv k_B T$, k_B is the Boltzmann constant and T is the system temperature. Once both f and h have been estimated, the product of the wetting coefficient and surface tension can be readily obtained as

$$k\gamma_{VL} = -\frac{1}{2L} \cdot \frac{f}{h} \qquad (10)$$

For a surface with a known value of k, Equation 10 can then be used to obtain the vapor-liquid surface tension, γ_{VL}. Similarly, for a liquid with a known γ_{VL}, k can be estimated using Equation 10.

5. Characteristic Features of SWIPES

The setup used in SWIPES is similar in spirit to the Wilhelmy plate method, which is a commonly-used experimental technique for determining $\gamma_{VL} \cos\theta$ [56,57]. In the experiments, the surface of interest (the Wilhelmy plate) is immersed in the liquid, and the capillary force it experiences is measured; here we bias the fluid to wet the surface instead, and measure the corresponding free energy change per unit length (f/h). The SWIPES approach is versatile, and can be used not only with Monte Carlo, but also with molecular dynamics simulations. It can be used to estimate both γ_{VL} and k for fluids and surfaces that vary widely in their cohesive and adhesive interaction strengths. Moreover, SWIPES is relatively easy to implement, and because it only requires estimates of ensemble averages that converge quickly, it is also computationally efficient. Another salient feature of SWIPES is that as the number of fluid molecules in v increases, the vapor-liquid interface moves along the solid surface, but no additional vapor-liquid interfacial area is created. In contrast, either vapor-liquid or vacuum-liquid interfaces are created in several computational approaches for estimating k, including the interface potential [34,39], phantom-wall [35,36], and dry-surface methods [37]. When carried out in the presence of periodic boundary conditions, the creation of such interfaces involves transitions between different dewetted morphologies, which can give rise to hysteresis effects, and complicate estimation of the corresponding free energies [48-51].

C. Molecular Models and Simulation Details

To illustrate our approach for estimating γ_{VL} and k, we study the wetting of a Lennard-Jones (LJ) solid surface by SPC/E water [55]. Following ref. 37, we study a family of surfaces composed of LJ atoms that vary in the strength of their interactions with water. The LJ atoms are placed on an FCC lattice with a spacing of 4.05 Å, and are restrained to their initial positions using harmonic springs with a spring constant of 1000 kJ/mol/nm^2. The (111) face of the LJ surface is placed in contact with water. The LJ interaction parameters for the solid atoms are $\sigma = 0.2629$ nm and $\varepsilon = 22.13$ kJ/mol.

The cross interaction between the solid atoms and water oxygens follows the Lorentz-Berthelot combining rule for σ, whereas the corresponding well-depth is systematically varied from $\varepsilon_{SW} = 0.001$ to 2.6 kJ/mol to tune surface-water interaction strength. The cutoff distance is chosen to be 1 nm for both the LJ potential and the real space electrostatic interactions. The reciprocal space electrostatic interactions are treated using particle mesh Ewald summation with a Fourier spacing of 0.1 nm [58]. The equations of motion are integrated using the leap-frog algorithm with a time step of 2 fs. The simulations are performed in the canonical ensemble, and the temperature of the system is set to 300 K using a Langevin thermostat with a coupling constant of 2 ps [59]. The SHAKE algorithm is used to constrain the internal degrees of freedom of the SPC/E water molecule [60]. All simulations were performed using GROMACS MD simulation package [61], which was modified in-house to incorporate the biasing potentials of interest. The biasing potentials described here have also been implemented in the open-source INDUS code, which can be accessed at: http://patelgroup.seas.upenn.edu/indus.html. The INDUS code implements the INDirect Umbrella Sampling method for biasing coarse-grained particle number as an extension to the PLUMED plugin, which interfaces with several popular MD simulation packages [62].

1. Biased Simulations

A solid surface consisting of 8640 particles is placed in contact with 7000 water molecules in a rectangular box with dimensions of 26.5 nm × 2.8059 nm × 14.319 nm (Figure 1). Additionally, a wall is placed at the left edge ($-x$) of the simulation box (not shown in Figure 1). The wall consists of 1200 particles that are arranged in four layers, and are constrained to occupy an FCC lattice with a spacing of 4.05 Å. The wall particles interact with water oxygens through the LJ potential with $\sigma = 0.29$ nm and a very small value of $\varepsilon = 0.001$ kJ/mol, which effectively makes the wall repulsive, enabling it to break translational symmetry and nucleate vapor in its vicinity. As illustrated in Figure 1, the left edge of the observation volume is placed roughly 1 nm to the left of the solid surface of interest, and the observation volume covers the entire surface. To obtain estimates of f and h, twelve biased simulations are performed with a fixed value of $\kappa = 0.05$ kJ/mol and different N^*-values that range from 4000 to 5100 in steps of 100. Each biased simulation is run for 1 ns, and the data from the first 400 ps are discarded as equilibration. For every biased simulation, $\tilde{N}_v$-values are stored every 50 time steps, whereas system configurations are saved every 500 time steps, and analyzed to obtain H. System configurations are additionally used to obtain vapor-liquid interface profiles; to this end, we average the water

density field over 600 configurations, and determine the iso-surface for which the averaged water density field is equal to half the bulk water density. The vapor-liquid interface profile thus obtained is fitted to a circle, and the tangent to the fitted circle at the solid surface, i.e., at the z-coordinate corresponding to the outmost layer of solid atoms, is used to obtain an estimate the contact angle, which we call θ_I. Error bars are estimated by dividing the production period into 3 to 5 blocks and determining the statistical uncertainty across the block averages.

2. Droplet Simulations for Estimating Contact Angles

To compare the wetting coefficients obtained using our approach with those obtained from the geometry of water droplets, we also perform simulations of (infinitely long) cylindrical water droplets on the LJ surfaces described above. In these simulations, the solid surface is composed of 4200 LJ atoms, and has dimensions of 17.3607 nm $\times$ 2.8059 nm $\times$ 1.2887 nm. A box with dimensions of 17.3607 nm $\times$ 2.8059 nm $\times$ 10.0 nm is used to simulate 2000 water molecules that are placed on the surface. The system is equilibrated for 4 ns, which is followed by a production period of 6 ns. In the production stage, configurations are collected every 1000 time steps, and are analyzed to characterize the shape of the droplet. Droplet interfaces, the corresponding contact angles (θ_D), and associated error bars are obtained as described above.

D. Results and Discussions

SWIPES is used to characterize the wetting coefficients (k) for LJ surfaces with wide range of solid-water attractions (ε_{SW}), and to estimate the vapor-liquid surface tension of water (γ_{VL}). The contact angles estimated using SWIPES (θ_F) are compared with those obtained using droplet geometries (θ_D). As ε_{SW} is increased, a transition from partial to complete wetting is observed. The computational efficiency of the method is also discussed.

1. Estimating wetting coefficients using SWIPES

To illustrate our method, we first estimate k for a surface with $\varepsilon_{SW} = 1.94$ kJ/mol. In Figure 2a, we show the ensemble averages of the coarse-grained number of waters, $\langle \tilde{N}_v \rangle_{\kappa,N^*}$, evaluated at different N^*-values. The data are fit well by a straight line with unit slope (dashed line), confirming that f is independent of N^* (Equation 8). The y-intercept of the fitted line corresponds to $-f/\kappa$, enabling estimation of $f = -0.143(3)$ kJ/mol. As shown in the Supplementary Information, estimates of f can also be obtained from individual biased simulations by using Equation 7, albeit with larger statistical uncertainties. Figure 2b shows that the position of vapor-liquid interface (H), quan-

tified by $\langle x_{COM} \rangle_{\kappa,N^*}$, varies linearly with N^*; the corresponding slope is $h = 8.6(2) \times 10^{-4}$ nm. As shown in the Supplementary Information, h can also be obtained from a single biased simulation by estimating the co-variance of x_{COM} and $\tilde{N}_v$ (Equation 9). However, due to the larger statistical uncertainties associated with co-variance estimation, the use of multiple biased simulations is likely to be more judicious route for estimating h. In Figure 2c, vapor-liquid interfaces identified from three biased simulations are shown with their x-coordinates shifted by $\langle x_{COM} \rangle_{\kappa,N^*}$; the excellent agreement between the shifted interfacial profiles highlights the fact that biasing potential moves the water slab along the solid surface, but does not otherwise influence the shape of the interface. Thus, Figure 2c further corroborates the linear dependences of both F_{κ,N^*} and $\langle x_{COM} \rangle_{\kappa,N^*}$ on N^*. With the corresponding slopes f and h estimated, k can then be obtained from Equation 10 if γ_{VL} is known. For the SPC/E water model used here, the surface tension has been estimated to be $\gamma_{VL}^{SPC/E} = 63.6(1.5)$ mN/m at 300 K[63]. With this value of surface tension, we estimate the wetting coefficient for the LJ surface with $\varepsilon_{SW} = 1.94$ kJ/mol to be $k = 0.78(2)$, and the corresponding contact angle to be $38(2)°$.

2. Estimating vapor-liquid surface tension using SWIPES

In principle, the vapor-liquid surface tension, γ_{VL}, of a fluid can be estimated using Equation 10 if we use SWIPES to characterize a surface (i.e., estimate f and h) for which the wetting coefficient is known. In practice, surfaces that are either fully wetting ($k = 1$) or non-wetting ($k = -1$) would work well for this purpose. However, purely repulsive surfaces are ideally suited for this purpose because they are non-wetting regardless of the fluid under consideration. Here, we use an effectively repulsive hydrophobic surface with $\varepsilon_{SW} = 0.001$ kJ/mol to estimate γ_{VL} for SPC/E water. For this surface, $\langle \tilde{N}_v \rangle_{\kappa,N^*}$ and $\langle x_{COM} \rangle_{\kappa,N^*}$ are shown as functions of N^* in Figures 3a and 3b, respectively. Using this data, we obtain estimates of f and h, which in turn enables us to estimate the vapor-liquid interfacial tension, $\gamma_{VL} = (1/2L) \cdot (f/h) = 64(2)$ mN/m. Our estimate is in excellent agreement with the value of 63.6 mN/m obtained in Ref. 63 using the test-area method.

3. LJ surfaces with a wide range of surface-water attractions

To highlight the versatility of SWIPES, we study surfaces with a wide range of solid-water interaction energies (ε_{SW}) that span an order of magnitude from roughly 0.2 to 2 kJ/mol. In each case, linear dependences of $\langle \tilde{N}_v \rangle_{\kappa,N^*}$ and $\langle x_{COM} \rangle_{\kappa,N^*}$ on N^* are observed; see Supplementary Information. The corresponding wetting coefficients are obtained using Equation 10, and are shown as a function of ε_{SW} in Figure 4a. Over this range of ε_{SW}-
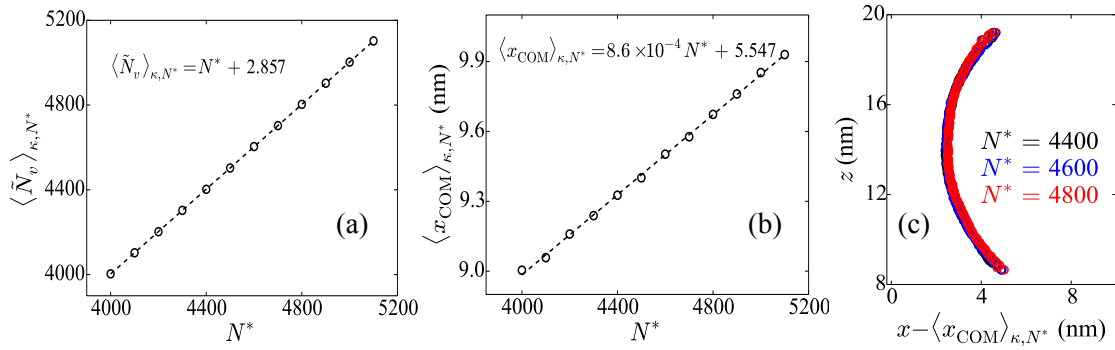
Fig. 2 Estimating the wetting coefficient for the LJ surface with $\varepsilon_{SW} = 1.94$ kJ/mol. (a) The average number of coarse-grained waters in the observation volume, $\langle \tilde{N}_v \rangle_{\kappa,N^*}$ increases with N^* (symbols). Following Equation 8, the data are fit to a straight line with unit slope (dashed line), and the intercept is used to estimate f. (b) The average x-position of the center of mass of the water slab, $\langle x_{COM} \rangle_{\kappa,N^*}$, also varies linearly with N^* (symbols); a linear fit to the data (dashed line) is used to obtain the slope, h. (c) Vapor-liquid interfaces, obtained from biased simulations with N^*-values of 4400, 4600 and 4800, are shifted in the x-direction by their respective $\langle x_{COM} \rangle_{\kappa,N^*}$-values. The shifted interfacial profiles (obtained by averaging over 1000 configurations) agree well with one another, suggesting that the biasing potential influences the position of the interface, but not its shape.
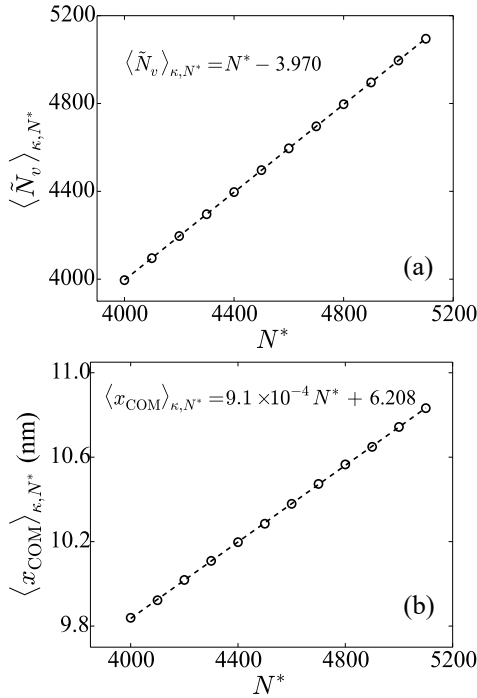

Fig. 3 Estimating the surface tension of SPC/E water using a non-wetting LJ surface with $\varepsilon_{SW} = 0.001$ kJ/mol. (a) The increase in $\langle \tilde{N}_v \rangle_{\kappa,N^*}$ with N^* (symbols), and a linear fit to the data (dashed line) are shown; in fitting the data, the slope is fixed at unity. (b) The variation of $\langle x_{COM} \rangle_{\kappa,N^*}$ with N^* (symbols), and a linear fit to the data (dashed line) are shown.

values, k increases monotonically with ε_{SW}, and varies from -0.92 to 0.91, nearly spanning the entire range of wetting coefficients possible.

The contact angle can also be estimated from our biased simulations by determining the angle between the surface and the tangent to the vapor-liquid interface at 3-phase contact. For the surface with $\varepsilon_{SW} = 1.94$ kJ/mol, the contact angle thus estimated is $\theta_I = 39(3)°$ (Figure 4b), in good agreement with the corresponding estimate $\theta_F =$

$38(2)°$ obtained using SWIPES. As described in detail in the Supplementary Information, we further estimated θ_F and θ_I using simulation setups with inter-surface separations that are smaller ($L_z = 10$ nm) and larger ($L_z = 17.2$ nm) than the separation used here ($L_z = 14.3$ nm), and found the estimates to also be within the statistical uncertainty. To compare our estimates of k with those obtained from the widely used sessile droplet method, we additionally simulate water droplets placed on the solid surfaces, and estimate the corresponding contact angles. Although spherical droplets are typically employed for this purpose, the corresponding results can depend on droplet size due to the influence of line tension. Following ref.[15], we thus make use of cylindrical droplets, which are infinitely long due to our use of periodic boundary conditions. For the surface with $\varepsilon_{SW} = 1.94$ kJ/mol, the droplet shape obtained from our simulations is shown in Figure 4c. Following the procedure described in section C, the droplet shape is used to estimate $\theta_D = 40(3)°$, which agrees well with both θ_F and θ_I. As shown in Figure 4a, such agreement between estimates of the wetting coefficients obtained from SWIPES (k_F) and those obtained from interfacial profiles (k_I) and droplets (k_D) is seen across the family of LJ surfaces with a wide range of ε_{SW}-values, suggesting that interface curvature effects are minimal (within the statistical uncertainty) for the LJ surfaces being studied here and for our choice of system sizes. The interfacial profiles used to estimate k_I and k_D are included in the Supplementary Information.

Such agreement may not always be observed, and is not expected in general; estimating k using SWIPES then offers three advantages over approaches that rely on droplet geometry. First, estimates of k_F are not expected to be influenced by line tension or interface curvature effects, as discussed in section B. In contrast, estimates of wetting co-
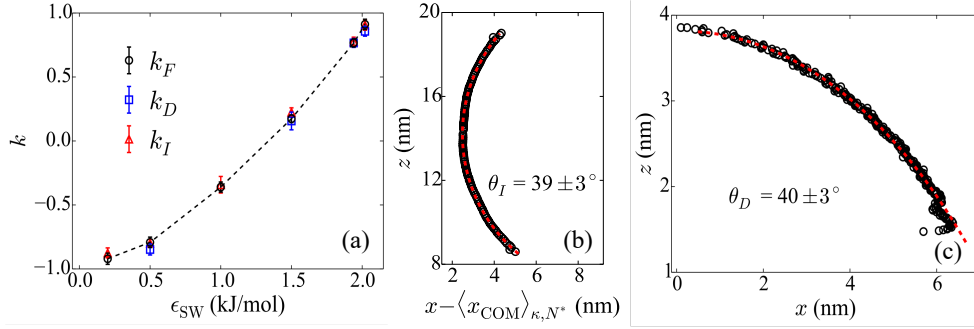
Fig. 4 (a) Wetting coefficients estimated using our free energy method (k_F) are shown for LJ surfaces with a wide range of ε_{SW}-values. These estimates are found to be consistent with the corresponding estimates obtained from the vapor-liquid interfacial profiles ($k_I \equiv \cos\theta_I$), as well as those obtained from separate simulations of cylindrical droplets ($k_D \equiv \cos\theta_D$). (b) For the LJ surface with $\varepsilon_{SW} = 1.94$ kJ/mol, the vapor-liquid interface obtained from a biased simulation with $N^* = 4800$ is shown (symbols). The interface is fit to a circle (red dashed line) and the contact angle θ_I is obtained from the tangent to the circle at 3-phase contact. (c) The shape of a cylindrical droplet placed on an LJ surface with $\varepsilon_{SW} = 1.94$ kJ/mol is shown. The droplet interface is fit to a circle (red dashed line) and the contact angle θ_D is obtained from the tangent to the circle at 3-phase contact.

efficients obtained using nanoscopic spherical droplets are expected to depend on droplet size due to line tension effects. Although the length of the 3-phase contact line is constant for cylindrical droplets, the corresponding contact angles can nevertheless depend on the curvature of the vapor-liquid interface. Second, the necessity of having to choose a contact plane introduces an inherent ambiguity in the determination of contact angle from geometric approaches [64–66]. Such ambiguity is expected to introduce systematic errors in k_I and k_D, which can only be eliminated by increasing droplet size. In contrast, the estimation of k_F is free from ambiguity, and uncertainties arise only from the sampling errors in estimating $\langle \tilde{N}_v \rangle_{\kappa,N^*}$ and $\langle x_{COM} \rangle_{\kappa,N^*}$. Accurate estimates of k_F can thus be obtained by simply increasing the number or length of the biased simulations. SWIPES may thus be better suited for studying small but important changes in wettability, such as the variations in k arising from small changes in pressure, fluid composition or surface chemistry. Lastly, the determination of contact angles from droplet geometry is challenging for both the most hydrophobic and the most hydrophilic surfaces. For hydrophobic surfaces with contact angles greater than 140°, the value of θ becomes increasingly sensitive to the choice of the contact plane, making its estimation from droplet geometry increasingly challenging. Conversely, for hydrophilic surfaces with contact angles below 30°, large system sizes and long equilibration times [28] are needed for droplets to spread on the surface and achieve their equilibrium shapes.

4. Fully Wetting and Dewetting Surfaces

As solid-fluid interactions become more favorable, θ decreases with the system eventually transitioning from partial wetting ($\theta > 0°$) to complete wetting ($\theta \to 0°$). Understanding the factors that govern transitions between partial and complete wetting states is of interest in diverse

contexts, including the design of materials, such as polymer nanocomposites [67–69]. Conversely, as solid-fluid interactions are made increasingly unfavorable, the fluid is expected to dewet the solid. Although the estimation of θ from droplet geometry becomes increasingly challenging for surfaces in the vicinity of wetting and dewetting transitions, here we illustrate that SWIPES nevertheless works well in those regimes.

An LJ surface with a small value of ε_{SW} interacts less favorably with liquid water than with its vapor phase, so that $\gamma_{SV} < \gamma_{SL}$, i.e., the surface is hydrophobic with $k = (\gamma_{SV} - \gamma_{SL})/\gamma_{VL} < 0$. As ε_{SW} is increased, the surface interacts more favorably with both the liquid and vapor phases of water, i.e., both γ_{SV} and γ_{SL} decrease; however, because the denser liquid can better utilize these favorable interactions, γ_{SL} decreases more rapidly than γ_{SV}, and the wetting coefficient, $k = (\gamma_{SV} - \gamma_{SL})/\gamma_{VL}$ increases. For a sufficiently large ε_{SW}-value, γ_{SL} eventually falls below γ_{SV}, i.e., the surface becomes hydrophilic with $k = (\gamma_{SV} - \gamma_{SL})/\gamma_{VL} > 0$. Eventually, as ε_{SW} is made large enough, any contact between solid and vapor is sufficiently unfavorable (relative to solid-liquid contact) that $k \to 1$ and $\gamma_{SV} \to \gamma_{SL} + \gamma_{VL}$. In this limit, the free energetic penalty for replacing the solid-vapor interface with a solid-liquid interface and a vapor-liquid interface vanishes, and water molecules from the vapor phase adsorb onto the surface to form a film of liquid. As ε_{SW} is increased even further, γ_{SL} does not continue to decrease more rapidly than γ_{SV}; rather the two quantities continue to decrease in concert with one another, so that k plateaus at 1. The phenomenology described above is generally true regardless of the solid and the fluid wetting it [52,70]. As shown in Figure 5a, SWIPES captures such a transition from partial wetting ($k < 1$) to complete wetting ($k = 1$) as ε_{SW} is increased, highlighting its suitability for characterizing highly hydrophilic surfaces. The ε_{SW}-value at which the wetting co-
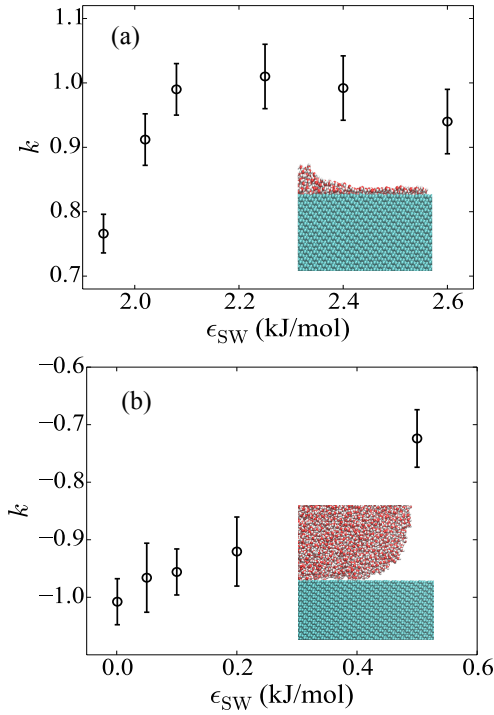
Fig. 5 (a) Wetting coefficients (k) are shown as a function of ε_{SW} in the vicinity of the transition from partial to complete wetting. The inset is a simulation snapshot focusing on the liquid film that forms on the LJ surface with $\varepsilon_{SW} = 2.4$ kJ/mol. (b) Wetting coefficients (k) are shown as a function of ε_{SW} near the transition from partial wetting to dewetting. The inset is a simulation snapshot focusing on the vapor layer that forms on the LJ surface with $\varepsilon_{SW} = 0.05$ kJ/mol.

efficient, k approaches 1 is roughly $\varepsilon_{SW}^* = 2.1$ kJ/mol, with a further increase in ε_{SW} leaving k unchanged. In the inset of in Figure 5a, we show a simulation snapshot of an LJ surface with $\varepsilon_{SW} = 2.4$ kJ/mol ($> \varepsilon_{SW}^*$) that is focused on the region near vapor-liquid-solid contact. The snapshot highlights the presence of water molecules that are adsorbed onto the solid surface, and form a liquid film which covers the surface.

In addition to the transition to complete wetting, SWIPES also captures the transition from partial wetting to dewetting as ε_{SW} is decreased. For small ε_{SW}-values, the surface is hydrophobic, and interacts more favorably with the vapor (relative to the liquid). For sufficiently small ε_{SW}, any contact between solid and liquid is so unfavorable (relative to solid-vapor contact) that the surface dewets forming a vapor layer adjacent to the surface, in a manner that is analogous to the formation of a liquid film in the complete wetting regime. The formation of such a vapor layer results in the solid-liquid interface being replaced with a solid-vapor interface and a vapor-liquid interface, and carries a vanishing free energetic penalty as $k \to -1$ and $\gamma_{SL} \to \gamma_{SV} + \gamma_{VL}$. As seen in Figure 5b, the wetting coefficient indeed approaches -1 for small ε_{SW}. In the inset of Figure 5b, a simulation

snapshot of a hydrophobic surface with $\varepsilon_{SW} = 0.05$ kJ/mol is shown; the region near the surface clearly shows the presence of a vapor layer.

An important feature of SWIPES is that both the liquid and vapor phases are always explicitly present by construction. This enables water molecules to adsorb onto the surface and form a liquid film in the complete wetting regime. Similarly, the surface is readily able to dewet and form a vapor layer in the dewetting regime. Moreover, because the vapor-liquid interface is moved along the surface in SWIPES, as surface area comes in contact with liquid, it simultaneously loses contact with the vapor, enabling direct estimation of $\gamma_{SV} - \gamma_{SL}$. In contrast, methods that involve replacing the liquid adjacent to the surface with a cavity or a vacuum [35,44] instead estimate $\gamma_{S,Vac} - \gamma_{SL}$. Because $\gamma_{S,Vac}$ does not depend on ε_{SW}, and γ_{SL} decreases monotonically with increasing ε_{SW}, their difference, $\gamma_{S,Vac} - \gamma_{SL}$ does not plateau with increasing ε_{SW}. Thus, such methods cannot identify the transition from partial to complete wetting unless $\gamma_{S,Vac} - \gamma_{SV}$ is estimated as well [51].

5. Computational Efficiency

In addition to being relative simple, SWIPES is also efficient from a computational standpoint. Here we provide a sense of the typical computational effort required to obtain accurate estimates of f and h, and thereby of k. As described in section B, the estimation of f relies on sampling of $\tilde{N}_v$, and an accurate estimation of its average, $\langle \tilde{N}_v \rangle_{\kappa, N^*}$ (Equation 7). Figure 6a shows the convergence of $\tilde{N}_v$ for two biased MD simulation with N^* of 4100 and 4500 for the LJ surface with $\varepsilon_{SW} = 1.94$ kJ/mol. As shown in Figure 6a, the cumulative average of $\tilde{N}_v - N^*$ (black line) converges to its equilibrium value (blue dashed line) in around 200 ps [71]. Similarly, Figure 6b shows the convergence of x_{COM} for the two biased simulations; the corresponding cumulative average converges to its equilibrium value in roughly 300 ps.

Although both f and h can also be estimated from individual biased simulations, the use of multiple simulations can yield estimates with lower statistical uncertainties. For the LJ surface with $\varepsilon_{SW} = 1.94$ kJ/mol, Figure 6c shows wetting coefficient (k) estimates and uncertainties calculated using an increasing number of biased simulations; every biased simulation has a production period of 600 ps, and the N^*-values of the biased simulations are separated by 100. Reasonably accurate estimates of k can be obtained with 3 to 6 biased simulations, suggesting that a total simulation time of roughly 5 ns is sufficient. This is comparable to the time needed to estimate contact angles from droplet shapes, and roughly an order of magnitude smaller than other free energy methods for estimating k, such as the procedure developed by Kanduc and Netz [52] or the dry-surface method [43],
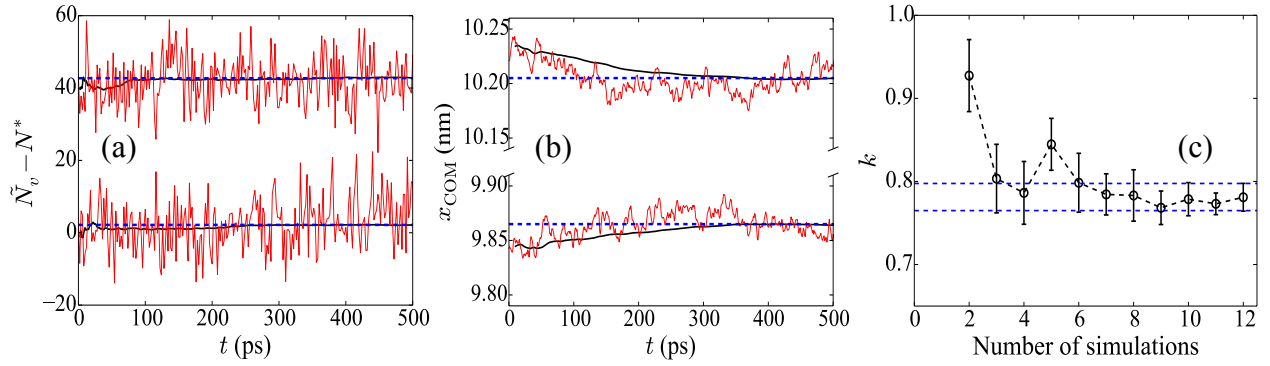
Fig. 6 For the LJ surface with ε_{SW} = 1.94 kJ/mol, the time dependences of (a) $\tilde{N}_v - N^*$ and (b) x_{COM} are shown for biased simulations with N^* = 4100 and N^* = 4500. The values of $\tilde{N}_v - N^*$ have been shifted up by 40 for the N^* = 4500 simulation for clarity. Instantaneous values (red line), cumulative averages (black line) and ensemble averages (blue dashed line) highlight that convergence is achieved in 200 - 300 ps. (c) Wetting coefficients (k) calculated using different number of simulations. Blue dashed lines correspond to the standard error obtained when all 12 simulations are used.

which require 20 or more simulations, each run for 2 ns or more. We thus expect SWIPES to be comparable with or more efficient than existing methods from a computational standpoint.

E. Conclusions and Outlook

In this work, we introduce a method for the characterization of surface wetting and interfacial properties using enhanced sampling. The method, which we call SWIPES, makes use of the indirect umbrella sampling (INDUS) technique to reversibly wet the surface of interest by biasing and systematically altering the coarse-grained number of fluid molecules in an observation volume v adjacent to the surface. SWIPES is versatile and can be used in conjunction with molecular dynamics simulations to estimate the wetting coefficient k (or equivalently the contact angle, θ) for systems with a wide range of solid-fluid interactions. It can also be used to estimate the vapor-liquid surface tension of a fluid by estimating the work required to wet a purely repulsive solvophobic surface. Importantly, SWIPES involves displacing a vapor-liquid interface along the solid surface, but not the creation of additional vapor-liquid interfacial area. In contrast, in a number of existing free energy methods, vapor-liquid interfaces spanning periodic boundaries are created; the creation of such interfaces involves transitions between different dewetted morphologies, which can give rise to hysteresis, and complicate estimation of the corresponding free energies[48–50].

We use SWIPES to characterize the wetting of a family of LJ surfaces by SPC/E water. For partially wetting surfaces with a wide range of attractions for water, our predictions for the contact angles are roughly consistent with those estimated from water droplet geometries. As the attractions between the solid surface and water are increased, SWIPES is able to capture the transition from partial to complete wetting; it can also captures the dewetting transition at low

attractions. Moreover, only ensemble averages of $\tilde{N}_v$ (number of fluid molecules in v) and x_{COM} (center of mass of fluid in the direction perpendicular to the vapor-liquid interface) are required, making SWIPES both straightforward to implement and computationally efficient; a total simulation time of roughly 5 ns is sufficient to obtain reasonably accurate estimates of k.

We note that although we have primarily discussed SWIPES in the context of surface-liquid-vapor systems, it can also be extended in a straightforward manner to other interfacial systems, such as surface-liquid-liquid or surface-liquid-solid systems. By biasing an appropriate order parameter to control the extent to which a surface is covered by one phase relative to another, the method presented here can be generalized to characterize the preference of a surface for one liquid over another, or for a crystalline solid over its coexisting liquid[40,72–74]. We further note that our approach can also be used to characterize the wettability of surfaces with nanoscale heterogeneities, such as chemically patterned surfaces or surfaces with nanoscale texture[75–81]. Although the wetting coefficient may not be well-defined for such surfaces, the free energy change upon wetting, ΔF, obtained using SWIPES, could nevertheless provide a useful description of surface wettability. The infiltration of fluids into porous media represents another important class of problems that could be studied using our approach[82,83]. Once again, SWIPES could be used to characterize the wettability of the pores through an estimation of the infiltration free energy.

Acknowledgements

References

1 K. L. Mittal, *Advances in Contact Angle, Wettability and Adhesion*, Scrivener Publishing LLC., 2013.

2 S. A. Deshmukh and S. K. Sankaranarayanan, *Phys. Chem. Chem. Phys.*, 2012, **14**, 15593–15605.

3 A. Y. Stark, I. Badge, N. A. Wucinich, T. W. Sullivan, P. H. Niewiarowski and A. Dhinojwala, *Proc. Natl. Acad. Sci. U.S.A.*, 2013, **110**, 6340–6345.

4 Y. Hu, D. Devegowda, A. Striolo, A. Phan, T. A. Ho, F. Civan and R. F. Sigal, *SPE J.*, 2014, **20**, 112–124.

5 A. Prakash, J. Pfaendtner, J. Chun and C. J. Mundy, *J. Phys. Chem. C*, 2017, **121**, 18496–18504.

6 K. Binder, D. Landau and M. Müller, *J. Stat. Phys.*, 2003, **110**, 1411–1514.

7 T. Ingebrigtsen and S. Toxvaerd, *J. Phys. Chem. C*, 2007, **111**, 8518–8523.

8 B. Shi and V. K. Dhir, *J. Chem. Phys.*, 2009, **130**, 034705.

9 S. Becker, H. M. Urbassek, M. Horsch and H. Hasse, *Langmuir*, 2014, **30**, 13606–13614.

10 A. Malani, A. Raghavanpillai, E. B. Wysong and G. C. Rutledge, *Phys. Rev. Lett.*, 2012, **109**, 184501.

11 T. Koishi, K. Yasuoka, S. Fujikawa and X. C. Zeng, *ACS Nano*, 2011, **5**, 6834–6842.

12 S. Tsuji, Y. Liang, M. Kunieda, S. Takahashi and T. Matsuoka, *Energy Procedia*, 2013, **37**, 5435 – 5442.

13 G. Javanbakht, M. Sedghi, W. Welch and L. Goual, *Langmuir*, 2015, **31**, 5812–5819.

14 C. Chen, B. Dong, N. Zhang, W. Li and Y. Song, *Energy Fuels*, 2016, **30**, 5027–5034.

15 C. M. Tenney and R. T. Cygan, *Environ. Sci. Technol.*, 2014, **48**, 2035–2042.

16 F. Jiménez-Ángeles and A. Firoozabadi, *J. Phys. Chem. C*, 2016, **120**, 11910–11917.

17 K. K. Bejagam, S. Singh and S. A. Deshmukh, *J. Comput. Chem.*, 2017, **39**, 721–734.

18 V. Kumar, S. Sridhar and J. R. Errington, *J. Chem. Phys.*, 2011, **135**, 184702.

19 F. Leroy and F. Mueller-Plathe, *J. Chem. Theory Comput*, 2012, **8**, 3724–3732.

20 A. Shahraz, A. Borhan and K. A. Fichthorn, *Langmuir*, 2013, **29**, 11632–11639.

21 J. Kerins and B. Widom, *The Journal of Chemical Physics*, 1982, **77**, 2061–2070.

22 F. Bresme, *Physical Review Letters*, 1998, **80**, 3791–3794.

23 J. H. Weijs, A. Marchand, B. Andreotti, D. Lohse and J. H. Snoeijer, *Phys. Fluids*, 2011, **23**, 022001.

24 H. Peng, G. R. Birkett and A. V. Nguyen, *Mol. Simul*, 2013, **40**, 934–941.

25 N. Giovambattista, A. B. Almeida, A. M. Alencar and S. V. Buldyrev, *The Journal of Physical Chemistry C*, 2016, **120**, 1597–1608.

26 A. B. Almeida, N. Giovambattista, S. V. Buldyrev and A. M. Alencar, *The Journal of Physical Chemistry C*, 2018, **122**, 1556–1569.

27 M. R. Slovin and M. R. Shirts, *Langmuir*, 2015, **31**, 7980–7990.

28 M. Kanduč, *J. Chem. Phys.*, 2017, **147**, 174701.

29 G. Scocchi, *Phys. Rev. E*, 2011, **84**, 061602.

30 M. Kanduč, *Phys. Rev. E*, 2018, **98**, 032804.

31 J. Škvára, J. Škvor and I. Nezbeda, *Mol Simul*, 2017, **44**, 190–199.

32 S. Ravipati, B. Aymard, S. Kalliadasis and A. Galindo, *J. Chem. Phys.*, 2018, **148**, 164704.

33 M. Khalkhali, N. Kazemi, H. Zhang and Q. Liu, *J. Chem. Phys.*, 2017, **146**, 114704.

34 E. M. Grzelak and J. R. Errington, *J. Chem. Phys.*, 2008, **128**, 014710.

35 F. Leroy and F. Müller-Plathe, *J. Chem. Phys.*, 2010, **133**, 044110.

36 F. Leroy, D. J. V. A. dos Santos and F. Müller-Plathe, *Macromol. Rapid Commun.*, 2009, **30**, 864–870.

37 F. Leroy and F. Müller-Plathe, *Langmuir*, 2015, **31**, 8335–8345.

38 X. Qi, Y. Zhou and K. A. Fichthorn, *The Journal of Chemical Physics*, 2016, **145**, 194108.

39 V. Kumar and J. R. Errington, *Mol. Simul*, 2013, **39**, 1143–1152.

40 W. Guo and J. R. Errington, *J. Phys. Chem. C*, 2018, **122**, 17309–17318.

41 F. Taherian, V. Marcon, N. F. A. van der Vegt and F. Leroy, *Langmuir*, 2013, **29**, 1457–1465.

42 H. Jiang, F. Müller-Plathe and A. Z. Panagiotopoulos, *J. Chem. Phys.*, 2017, **147**, 084708.

43 F. Leroy, *J. Chem. Phys.*, 2016, **145**, 164705.

44 A. J. Patel, P. Varilly, S. N. Jamadagni, H. Acharya, S. Garde and D. Chandler, *Proc. Natl. Acad. Sci. U.S.A.*, 2011, **108**, 17678–17683.

45 K. Binder, B. J. Block, P. Virnau and A. Tröster, *Am. J. Phys.*, 2012, **80**, 1099–1109.

46 R. C. Remsing, E. Xi, S. Vembanur, S. Sharma, P. G. Debenedetti, S. Garde and A. J. Patel, *Proc. Natl. Acad. Sci. U.S.A.*, 2015, **112**, 8181–8186.

47 S. Prakash, E. Xi and A. J. Patel, *Proc. Natl. Acad. Sci. U.S.A.*, 2016, **113**, 5508–5513.

48 R. Godawat, S. N. Jamadagni, J. R. Errington and S. Garde, *Ind. Eng. Chem. Res.*, 2008, **47**, 3582–3590.

49 L. G. MacDowell, V. K. Shen and J. R. Errington, *J. Chem. Phys.*, 2006, **125**, 034705.

50 E. M. Grzelak and J. R. Errington, *Langmuir*, 2010, **26**, 13297–13304.

51 M. Kanduč and R. R. Netz, *J. Chem. Phys.*, 2017, **146**, 164705.

52 M. Kanduč and R. Netz, *Proc. Natl. Acad. Sci. U.S.A.*, 2015, **112**, 12338–12343.

53 A. J. Patel, P. Varilly and D. Chandler, *J. Phys. Chem. B*, 2010, **114**, 1632–1637.

54 A. J. Patel, P. Varilly, D. Chandler and S. Garde, *J. Stat. Phys.*, 2011, **145**, 265–275.

55 H. J. C. Berendsen, J. R. Grigera and T. P. Straatsma, *J. Chem. Phys.*, 1987, **91**, 6269–6271.

56 H. Butt, K. Graf and M. Kappl, *Physics and Chemistry of Interfaces*, Wiley., Weinheim, Germany, 2003.

57 A. Alghunaim, S. Kirdponpattara and B.-m. Z. Newby, *Powder Technology*, 2016, **287**, 201–215.

58 D. Frenkel and B. Smit, *Understanding Molecular Simulation From Algorithms to Applications*, Academic Press, Orlando, FL, USA., 2001.

59 T. Schneider, *Phys. Rev. B*, 1978, **17**, 1302–1322.

60 J.-P. Ryckaert, G. Ciccotti and H. J. Berendsen, *J. Comput. Phys.*, 1977, **23**, 327 – 341.

61 B. Hess, C. Kutzner, D. van der Spoel and E. Lindahl, *J. Chem. Theory Comput.*, 2008, **4**, 435–447.

62 M. Bonomi, D. Branduardi, G. Bussi, C. Camilloni, D. Provasi, P. Raiteri, D. Donadio, F. Marinelli, F. Pietrucci, R. A. Broglia and M. Parrinello, *Comput. Phys. Commun.*, 2009, **180**, 1961–1972.

63 C. Vega and E. de Miguel, *J. Chem. Phys.*, 2007, **126**, 154707.

64 B. Rotenberg, A. J. Patel and D. Chandler, *J. Am. Chem. Soc.*, 2011, **133**, 20521–20527.

65 D. Sergi, G. Scocchi and A. Ortona, *Fluid Ph. Equilibria*, 2012, **332**, 173–177.

66 S. Iglauer, M. Mathew and F. Bresme, *J. Colloid Interface Sci.*, 2012, **386**, 405–414.

67 S. K. Kumar, N. Jouault, B. Benicewicz and T. Neely, *Macromolecules*, 2013, **46**, 3199–3214.

68 T. B. Martin, K. I. S. Mongcopa, R. Ashkar, P. Butler, R. Krishnamoorti and A. Jayaraman, *J. Am. Chem. Soc.*, 2015, **137**, 10624–10631.

69 R. C. Ferrier Jr, J. Koski, R. A. Riggleman and R. J. Composto, *Macromolecules*, 2016, **49**, 1002–1015.

70 K. Binder, *Annu. Rev. Mater. Res.*, 2008, **38**, 123–142.

71 A. J. Patel and S. Garde, *J. Phys. Chem. B*, 2014, **118**, 1564–1573.

72 H. Fan, D. E. Resasco and A. Striolo, *Langmuir*, 2011, **27**, 5264–5274.

73 X.-C. Luu and A. Striolo, *J. Phys. Chem. B*, 2014, **118**, 13737–13743.

74 S. M. Marks and A. J. Patel, *Proc. Natl. Acad. Sci. U.S.A.*, 2018, **115**, 8244–8246.

75 N. Giovambattista, C. F. Lopez, P. J. Rossky and P. G. Debenedetti, *Proc. Natl. Acad. Sci. U.S.A.*, 2008, **105**, 2274–2279.

76 H. Acharya, S. Vembanur, S. N. Jamadagni and S. Garde, *Faraday Discuss.*, 2010, **146**, 353–365.

77 A. J. Patel, P. Varilly, S. N. Jamadagni, M. F. Hagan, D. Chandler and S. Garde, *J. Phys. Chem. B*, 2012, **116**, 2498–2503.

78 R. C. Harris and B. M. Pettitt, *Proc. Natl. Acad. Sci. U.S.A.*, 2014, **111**, 14681–14686.

79 E. Xi, V. Venkateshwaran, L. Li, N. Rego, A. J. Patel and S. Garde, *Proc. Natl. Acad. Sci. U.S.A.*, 2017, **114**, 13345–13350.

80 J. Wang, D. Bratko and A. Luzar, *Proc. Natl. Acad. Sci. U.S.A.*, 2011, **108**, 6374–6379.

81 R. C. Remsing, E. Xi and A. J. Patel, *J. Phys. Chem. B*, 2018, **122**, 3635–3646.

82 Y.-R. Huang, Y. Jiang, J. L. Hor, R. Gupta, L. Zhang, K. J. Stebe, G. Feng, K. T. Turner and D. Lee, *Nanoscale*, 2015, **7**, 798–805.

83 A. Shavit and R. A. Riggleman, *Soft Matter*, 2015, **11**, 8285–8295.